Strange metal behavior of the Hall angle in twisted bilayer graphene

Rui Lyu, ¹ Zachary Tuchfeld, ¹ Nishchhal Verma ¹, ¹ Haidong Tian, ¹ Kenji Watanabe, ² Takashi Taniguchi, ² Chun Ning Lau, ¹ Mohit Randeria, ¹ and Marc Bockrath ^{1,*}

¹ Department of Physics, The Ohio State University, Columbus, Ohio 43210, USA

² National Institute for Materials Science, Namiki Tsukuba Ibaraki 305-0044, Japan

(Received 17 February 2021; revised 4 May 2021; accepted 17 May 2021; published 17 June 2021)

Twisted bilayer graphene (TBG) with interlayer twist angles near the magic angle $\approx 1.08^{\circ}$ hosts flat bands and exhibits correlated states including Mott-like insulators, superconductivity, and magnetism. A linear-intemperature normal state resistivity in TBG has been attributed to an exotic Planckian dissipation mechanism but can be equally well explained in terms of conventional electron-phonon scattering. To address this issue, we perform combined temperature-dependent transport measurements of both the longitudinal and Hall resistivities in near-magic-angle TBG. While the observed longitudinal resistivity follows linear temperature T dependence consistent with previous reports, the Hall resistance shows an anomalous T dependence with the cotangent of the Hall angle $\cot \Theta_H \propto T^2$. Boltzmann theory for quasiparticle transport predicts that both the resistivity and $\cot \Theta_H$ should have the same T dependence, contradicting the observed behavior. This failure of quasiparticle-based theories is reminiscent of other correlated strange metals such as cuprates.

DOI: 10.1103/PhysRevB.103.245424

I. INTRODUCTION

Transport in strongly correlated systems, where electronic quasiparticle excitations are not well defined, has attracted attention in diverse areas of physics ranging from quantum materials [1,2] and cold atoms [3] to string theory [4]. Many of these investigations have their roots in the first observation of resistivity scaling linearly with temperature T in the normal state of high-temperature cuprate superconductors, along with a host of other anomalies including the T^2 scaling of cotangent of the Hall angle Θ_H [5,6], which remain challenging open problems to this day.

Magic-angle twisted bilayer graphene (TBG) has emerged as a system exhibiting a wealth of tunable many-body phases [7–17]. Moreover, the discovery of superconducting domes in the vicinity of correlated insulating phases [8,9] shows that this system shares features with the high T_c cuprate phase diagram [9]. Nevertheless, there are many differences with the cuprates: the TBG electronic structure has multiple bands crossing the Fermi energy, Berry phase effects, and Dirac dispersion. There are also differences in the phenomenology, such as the observation of nearby ferromagnetic phases [7,12,13]. In view of this, it is important to understand the normal state transport phenomenology in TBG. Based on the linear T resistivity, Cao et al. [18] have suggested that magicangle TBG exhibits exotic "Planckian dissipation" [19] like the cuprates. However, as many common metals show linear T resistivity, authors of other work [20,21] have interpreted this behavior within a conventional electron-phonon scattering picture [22]. Therefore, resistivity measurements alone are unable to determine the mechanism of scattering in TBG close to the magic angle.

In this paper, we present weak-field Hall resistivity and cotangent of the Hall angle measurements that, along with theoretical arguments, add crucial insights to this story and enable the two scenarios to be distinguished. Our main goal here is to address the question: can we understand both the observed longitudinal and Hall resistivities ρ_{xx} and ρ_{xy} within a conventional textbook picture of metallic transport, or do the experiments imply an exotic transport regime characteristic of correlated quantum matter?

Here, we study devices based on TBG with interlayer twist angles near the magic twist angle $\approx 1.08^{\circ}$. The longitudinal resistivity shows $\rho_{xx} \propto T$ over a range of temperatures from 10 to 100 K. At higher temperatures, we typically observe a resistivity maximum at a characteristic temperature $T_{\text{max}} \approx 100-200$ K. The Hall resistance ρ_{xy} is temperature dependent, such that $\cot \Theta_H = \rho_{xx}/\rho_{xy} \propto T^2$ for the range over which the resistivity is T linear.

While the linear T ρ_{xx} behavior can be consistent with electronic quasiparticle scattering by phonons, we find that this conventional picture cannot even qualitatively explain the Hall transport. Quite generally, in Boltzmann theory, $\rho_{xx} \propto 1/\tau$, where τ is the transport scattering rate, while $\cot \Theta_H = (\omega_c \tau)^{-1}$, where ω_c is the cyclotron frequency. Thus, both ρ_{xx} and $\cot \Theta_H$ should exhibit identical T dependence, arising from a common scattering rate (see Appendix G). The observed $\cot \Theta_H \propto T^2$ behavior in the density and temperature regime, where $\rho_{xx} \propto T$, is simply inconsistent with any quasiparticle-based transport theory. We note that this is the same dichotomy found in the strange metal regime of high T_c cuprates [5,6].

II. DEVICE FABRICATION

Samples were made using the "tear-and-stack" technique on a custom-made micropositioning stage like the method reported in Refs. [9,23,24]. TBG stack, with a small twist

^{*}Corresponding author: Bockrath.31@osu.edu

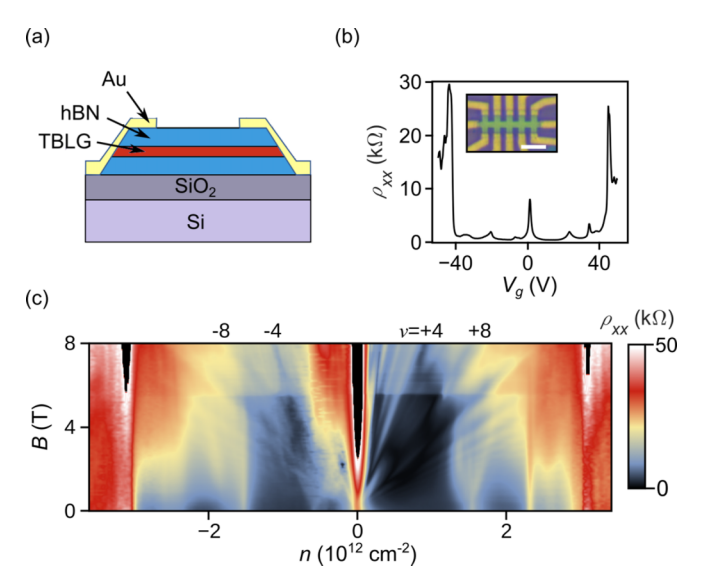


FIG. 1. Twisted bilayer graphene (TBG) device geometry and electronic transport measurements. (a) Schematic of layer stack geometry showing a BN-encapsulated TBG with attached gate and contact electrodes. (b) Plot of ρ_{xx} vs n for a sample D1 with twist angle $\approx 1.15^{\circ}$ taken at T=1.5 K. Inset: optical image of D1, scale bar 4 μ m. (c) Color plot of $\rho_{xx}(n,B)$ showing Landau fan features for sample D1. Color scale is nonlinear to enhance contrast. Filling factors for several minima originating from charge neutrality are shown above the plot. Black regions at charge neutrality and full filling occurring at nonzero B result from amplifier saturation.

angle $\sim 1-2^\circ$ were produced by tearing a graphene flake and rotating and stacking the separated pieces on top of each other. A larger angle than intended was targeted because, typically, the angle as measured from transport data is smaller due to interlayer relaxation [9,23,24]. Figure 1(a) shows a schematic diagram of a layer stack with the hexagonal BN-encapsulated device along with the oxidized Si wafer, which acts as a gate electrode to modulate the charge density. The stacks were then etched into a Hall bar geometry and Cr/Au edge contacts attached by electron beam lithography. A device optical image with attached electrodes is shown in the Fig. 1(b) inset.

III. EXPERIMENTAL RESULTS AND DISCUSSION

Completed samples were loaded into a flowing He gas cryostat, and transport measurements were performed. Figure 1(b) shows the longitudinal resistivity ρ_{xx} vs gate voltage V_g at the base temperature of 1.5 K for a device D1. Large peaks are observed near charge neutrality as well as near $V_g \approx \pm 45$ V. This agrees with previous measurements where, because of the moiré superlattice produced by the interlayer twist, flat bands develop near charge neutrality, with an energy gap separating these bands from dispersive bands. When four electrons per moiré unit cell are added or removed, the Fermi level reaches the energy gap, producing the observed resistance peaks.

The evolution of these peaks with magnetic field is shown in Fig. 1(c), with Landau fan features emanating from charge neutrality as well as several other zero-field peaks. Based on an analysis of these data, we find a gate capacitance of $C_g = 1.12 \times 10^{-4} \, \text{F/m}^2$. This enables us to determine the car-

rier density to fill the flat bands as $n_0 \approx \pm 3.1 \times 10^{12}$ cm⁻² and plot the horizontal axis as the density n. Filling factors for some of the main ρ_{xx} minima near n=0 are shown along the top of Fig. 1(c). From the measured n_0 , we infer an interlayer twist angle $\sim 1.15^{\circ}$ [8,9]. Low-temperature peaks in ρ_{xx} also occur for normalized values of the density $\sim n = n/n_0$ near $-\frac{1}{4}$, $\pm \frac{1}{2}$, and $\pm \frac{3}{4}$. These peaks correspond to correlated insulating states found previously [7–17].

Figure 2(a) shows a color plot of the longitudinal resistivity ρ_{xx} vs n and T, while Fig. 2(b) shows ρ_{xy} vs n and T. Resistivity ρ_{xx} vs T traces extracted from Fig. 2(a) at different densities corresponding to the vertical dashed lines in Fig. 2(a) are shown by the blue, black, and red triangles in Fig. 2(c). Data from two other devices D2 and D3, with twist angles ~ 1.1 and $\sim 0.91^{\circ}$, respectively, [similar color plots to Figs. 2(a) and 2(b) are shown in Appendix A] are shown by the circles and squares taken at several different densities near half-filling. The black dashed lines show that, above a coherence temperature [18] $T \approx 5-10$ K, ρ_{xx} increases linearly with temperature for each device. Figure 2(d) shows ρ_{xy} data for D1–3 taken at the same densities as ρ_{xx} for each sample. The sign of ρ_{xy} at half-filling depends on the sign of the effective mass and hence the twist angle, see Appendix C. For all the samples at sufficiently high T, $|\rho_{xy}|$ shows a decreasing trend with temperature. We note that work on epitaxial graphene observed significant density shifts at fixed gate voltage $> \sim 100 \, \mathrm{K}$ due to thermally activated charge traps [25], which could also cause changes in ρ_{xy} . However, in Fig. 2(a), the resistivity peaks occur at fixed $V_{\rm g} > \sim 10\,{\rm K}$ (the *n* axis is determined from V_g only by a scale factor), directly confirming that the temperature does not affect the charge density in this regime. This is consistent with the much smaller concentration of charge traps expected in BN-encapsulated devices [26] that we measure, while additionally Fig. 2 shows $T < 100 \,\mathrm{K}$ data.

After a linear T increase, ρ_{xx} reaches a broad maximum before turning downwards. This behavior is shown in Fig. 3(a) for sample D2, which shows maxima at a characteristic temperature which decreases as the doping increases toward $n/n_0 = 4$. We attribute this maximum to activation of carriers in higher energy bands, in agreement with Ref. [20], along with a \sim 5–10 meV rise in chemical potential. In Fig. 3(b), we plot the band structure from Ref. [27], which goes beyond the original continuum model [27-29] and includes structural relaxation that leads to a significant gap between the flat and dispersive bands. At the measured twist angle for D2 of $\sim 1.1^{\circ}$, this shows a narrow band with bandwidth $W \approx 40$ meV. The right panel of Fig. 3(b) shows the corresponding density of states. The Fermi function is plotted for $T = 150 \,\mathrm{K}$ at a density $n = 1.5 \times 10^{12} \,\mathrm{cm}^{-2}$ as the blue dashed line in Fig. 3(b). As the full width at half maximum of the Fermi function energy derivative $\approx 3.5k_BT$, we expect the excited band to begin being populated when $3.5 k_B T \approx W$, yielding $T \approx 130$ K, in good agreement with the observed 150 K near half filling. The density dependence of the resistivity maximum can also be understood using this band structure (see Appendix C).

We now turn to linear T variation of our resistivity in terms of various models. We know that two-dimensional (2D) resistivity is $\sim (h/e^2)(k_F l)^{-1}$, where k_F is the Fermi wave vector, and l is the inferred electronic mean free path. The measured

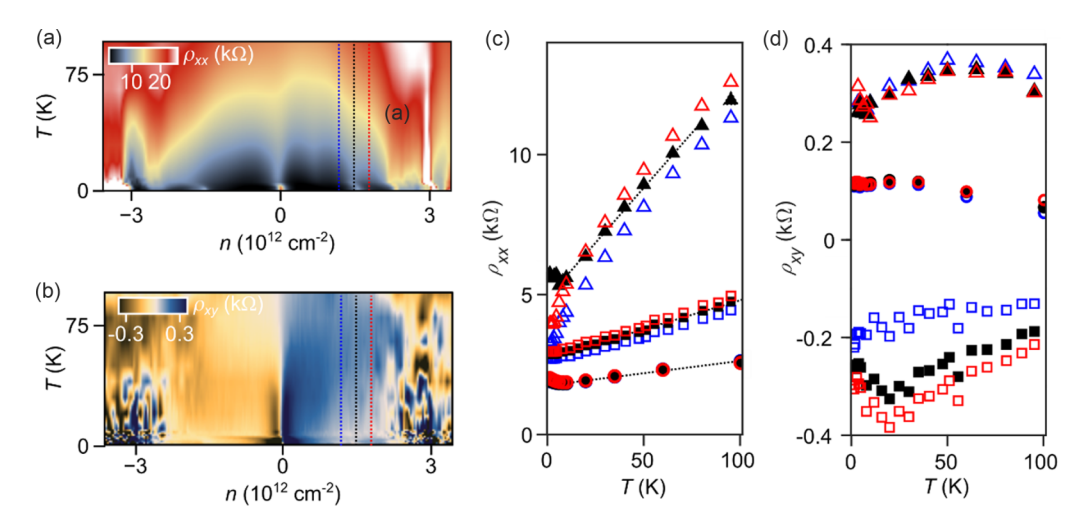


FIG. 2. Longitudinal and Hall resistivity of twisted bilayer graphene (TBG) devices. (a) Color plot of resistivity ρ_{xx} vs temperature T and density n taken from sample D1. (b) Color plot of resistivity ρ_{xy} vs T and n, taken at a magnetic field B=0.3 T. Similar color plots to (a) and (b) are shown in Figs. 5 and 6 for sample D2 and D3, respectively. (c) Line traces of ρ_{xx} for three samples. The triangles, squares, and circles indicate data taken from D1 (twist angle $\approx 1.15^{\circ}$), D2 (twist angle $\approx 1.10^{\circ}$), and D3 (twist angle $\approx 0.91^{\circ}$), respectively, with the line traces for D1 having the corresponding colors shown in (a). For clarity, D1 data have been offset upwards by 2 k Ω , while D2 data are shifted upwards by 1 k Ω . Filled symbols indicate data taken near half-filling, while open symbols indicate data taken away from half-filling. The dashed lines show linear fits to the half-filling data, yielding slopes of 79, 18, and 8.8 Ω/K for D1, D2, and D3, respectively. (d) Transverse resistivity ρ_{xy} for the same three samples with data for D1 taken at B=0.3 T for D1 and D3, and B=0.2 T for D2. Data for D1 and D3 were obtained using a contact symmetrization procedure, while a background was subtracted from D2 to compensate for an apparent mixing of ρ_{xx} into ρ_{xy} , see Appendix A. D1 data (triangles) have been shifted upward by 0.2 k Ω for clarity.

resistivity in our experiment is $\ll (h/e^2) = 25.81 \,\mathrm{k}\Omega$ in the relevant temperature range. Thus, TBG is not obviously in a "bad metal" regime where the Mott-Ioffe-Regel (MIR) limit is violated with $k_F l \approx 1$ and the quasiparticle picture necessarily breaks down. It makes sense to ask if we can understand TBG transport within a conventional Boltzmann formalism of weakly interacting quasiparticles.

The very narrow bandwidth inferred theoretically and from our data is consistent with previous reports [7–13,27–29].

This raises the possibility that T variations of the density of states as determined by the compressibility $dn/d\mu$ (where n is the electron density, and μ is the chemical potential), negligible in conventional metals, might be important for transport in magic-angle TBG. This impacts transport in narrow bands through the energy derivative of the Fermi function and through the T dependence of μ , even if the quasiparticle scattering rate (from impurities) is T independent. Such effects become significant when k_BT is of the order of the bandwidth.

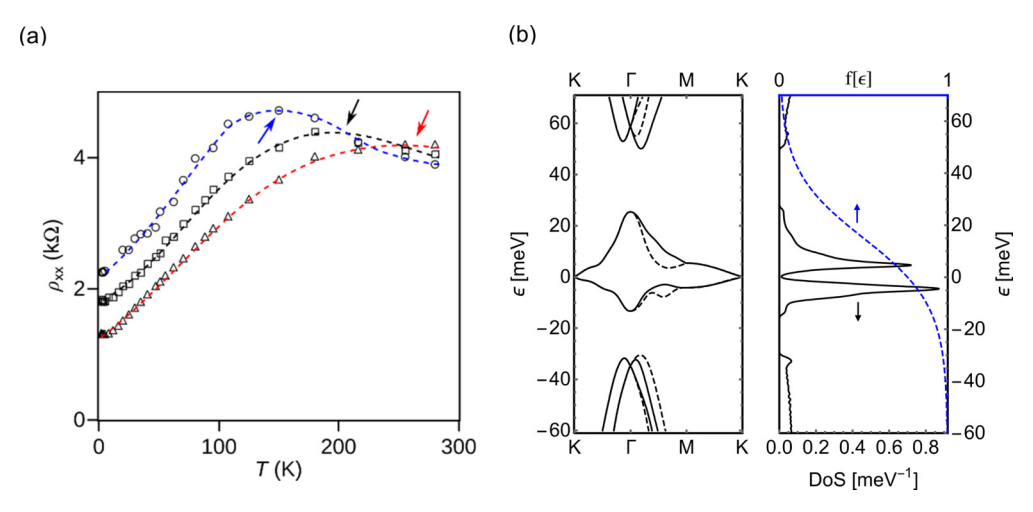


FIG. 3. Temperature dependence of resistivity and theoretical model. (a) ρ_{xx} vs T up to higher temperatures for D2, taken at densities $n = 0.96 \times 10^{12}$, 1.4×10^{12} , and 1.64×10^{12} cm⁻² (triangles, squares, circles, respectively). The red, black, and blue dashed lines are guides to the eye connecting data for each density. Each data trace shows a maximum at a temperature T_{max} shown by the arrow with the corresponding color to each guide that decreases with density. (b) Calculated band structure for a twist angle 1.1° following Ref. [27]. The band structure comes with an estimate of the energy gap between the narrow and higher bands. The peak in resistivity can be understood as the activation of carriers in higher bands due to thermal broadening of the Fermi function step along with the chemical potential shift. Blue dashed line shows the Fermi function centered at chemical potential corresponding to density 1.5×10^{12} cm⁻², with T = 150 K.

However, using realistic band structure parameters, we find that these effects are not relevant for the linear *T* resistivity between 10 and 100 K (see Appendix D).

Next, we consider electron-phonon scattering, which accounts for linear T resistivity in many metals over a range of temperatures $T_{\min} < T < T_{\max}$ with T_{\max} determined by the MIR criterion and T_{\min} set by the Debye temperature. This mechanism is not responsible for the linear T resistivity in strongly correlated materials dubbed "strange metals" [1,2]. Such materials often violate the MIR criterion with no apparent T_{\max} for linear resistivity, and T_{\min} is often too low to be consistent with phonons. We emphasize that TBG is different on both counts. First, the MIR criterion is never violated in TBG because of its multiband nature, as discussed above. Second, as emphasized in Ref. [22], a very low $k_B T_{\min} \approx \hbar \omega(Q)$ can arise in low-density materials (with small k_F), where $\omega(Q)$ is the phonon frequency at momentum transfer $Q = 2k_F$.

We can fit ρ_{xx} data treating electron-phonon scattering [22] within a Boltzmann approach. The scattering rate $1/\tau$ acquires a linear T dependence from the phonon occupation for $k_B T > \hbar \omega(2k_F)$, and thus, $\rho_{xx} \approx 1/\tau \approx T$. A quantitative fit to the slope can be obtained using the result ρ_{xx} = $\pi F D^2 k_B T / g e^2 \hbar \rho_m v_F^2 v_a^2 + \rho_0$, where D is the deformation potential, v_F and v_a are the Fermi and acoustic phonon velocities, ρ_m is the sheet mass density of graphene, g = 4 is the band degeneracy, ρ_0 is a constant representing the residual resistance from impurity scattering, and F is a dimensionless factor that depends on the twist angle [22]. These fits are shown in Fig. 2(c) as the dashed lines, and the parameter values are consistent with previous reports [20,22] and with that expected for v_F from the band structure of Fig. 3(b) for all three samples ($v_F = 3.6 \times 10^4, 7 \times 10^4, 1 \times 10^5 \,\text{m/s}$ for D1, D2, and D3, respectively). Momentum dependence of the matrix elements and occupancy factors are only important in temperatures $< T_{BG}$ and lead to a smooth crossover to a $\sim T^4$ regime. The phonon model does exceptionally well in capturing the said crossover (see Appendix E).

We now turn to the predictions of the electron-phonon model for the Hall response. Figure 2(d) shows the measured $\rho_{xy}(T)$, which is certainly not the T-independent response one expects in a simple metal. It is instructive to analyze our transport data in terms of the Hall angle $\cot \Theta_H = \rho_{xx}/\rho_{xy}$, which within Boltzmann theory has the simple expression $\cot \Theta_H = (\omega_c \tau)^{-1}$ (see Appendix F). Recalling Matthiessen's rule that the total scattering rate is the impurity scattering rate (which determines the T=0 intercept) plus the inelastic T-dependent scattering rate, we subtract out the T=0 value of the cotangent of the Hall angle and plot $\Delta \cot \Theta_H(T)$ in Fig. 4.

The inset of Fig. 4 shows the measured $\Delta \cot \Theta_H(T)$ vs T, which has a quadratic temperature dependence (dashed line), while the electron-phonon theory leads to a linear T dependence (blue line). The quadratic variation of $\Delta \cot \Theta_H(T)$ in all our devices is further emphasized in Fig. 4, where we plot our data from all three samples vs T^2 . Additional data are shown in Appendix A. The data follow a linear trend in the plot over the temperature range in which T linear ρ_{xx} behavior is observed.

We find that, while electron-phonon scattering can indeed account for the linear T longitudinal resistivity, it fails to explain the observed quadratic behavior of $\cot \Theta_H$. We emphasize that this problem is not limited to electron-phonon

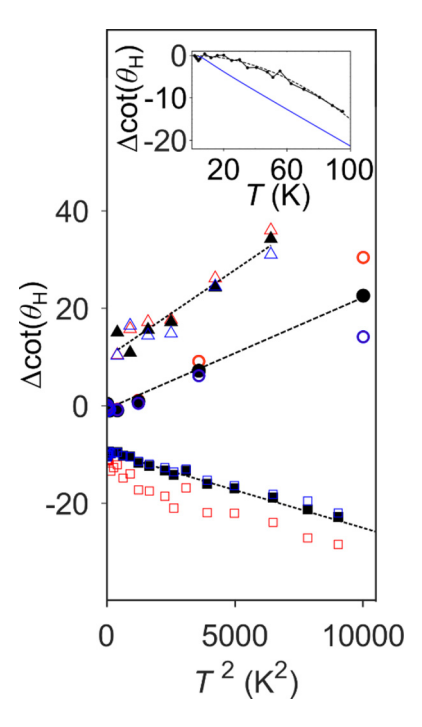


FIG. 4. Temperature dependence of the cotangent of the Hall angle. Main panel: Change in the cotangent of the Hall angle from its low-temperature value vs T^2 . Triangles represent data from D1, squares from D2, and circles from D3. Colors for D1 correspond to those in Fig. 2. Data for D2 and D3 are taken at similar band filling factors. Filled symbols indicate data taken near half-filling, while open symbols indicate data taken away from half-filling. The dashed lines show linear fits to the half-filling data. Inset: measured change in cot Θ_H vs T near half-filling for D2 on a linear scale. Blue line shows the trend expected from a theory calculation using phonon scattering.

scattering per se but points to a deeper failure of Boltzmann theory of quasiparticle transport. Within this theory, if the same scattering mechanism influences both longitudinal and Hall conductivities, even with arbitrary momentum and banddependent scattering rates (see Appendix G), ρ_{xx} and cot Θ_H will have the same T dependence. One might consider thermal activation of carriers in higher energy bands for a plausible explanation. However, as seen in resistivity measurements, these effects set in \sim 150 K. Moreover, they do not lead to the T^2 dependence observed in our devices. In sum, Boltzmann theory is clearly at odds with our measurements. Finally, we note that we expect conventional quasiparticle transport found in monolayer graphene up to room temperature [30] to be recovered for sufficiently large twist angles, due to the expected [28] and observed [31] decoupling of the layers in the large angle regime. Future work will be necessary to determine how conventional quasiparticle behavior emerges as the twist angle is increased. Nevertheless, our devices clearly demonstrate nonconventional behavior of cot Θ_H vs T for angles near the magic angle.

IV. CONCLUSION

We are forced to conclude that the totality of transport data in our devices cannot be understood in terms of conventional quasiparticle transport theory and appears to be very similar to the still unsolved problem of normal state transport in high T_c cuprate superconductors and other strongly correlated systems. This provides further support for the notion that correlations remain important in the normal metal phase above T_c and may provide some insight into the mechanism of the formation of the correlated phases.

Our results raise the question of why quasiparticle transport theory breaks down in TBG near the magic angle. Vicinity to a quantum critical point (QCP) can account for the absence of a scale—other than the temperature k_BT —in the scattering rate \hbar/τ since all other energy scales collapse to zero. QCPs are a common feature of many of the correlated materials where similar transport anomalies have been seen. They are well established in heavy fermion materials [32] and Fe-based superconductors [33]. There is mounting evidence in cuprates as well [34,35]; however, its nature is less understood. Thus, an important open question is whether there is an underlying QCP in magic-angle TBG that controls the anomalous power laws seen in our transport data.

ACKNOWLEDGMENTS

The experimental portion of this paper was funded by the Department of Energy under Award No. DE-SC0020187. N.V. and M.R. were supported by the Center for Emergent Materials, an NSF-funded MRSEC under Grant No. DMR-1420451 and No. DMR-2011876.

R.L., Z.T., N.V., and H.T. contributed equally to this paper.

APPENDIX A: ADDITIONAL DATA AND ANALYSIS OF ρ_{xy} DATA

Additional transport data are shown in Figs. 5 and 6, respectively. Figure 6(c) shows the change in $\cot \Theta_H$ vs T for device D1 for hole doping at several densities near half-filling. These data also follow a T^2 dependence. For sample D2, an apparent offset in ρ_{xy} was corrected for each gate voltage sweep by averaging the data over a range of charge densities n near charge neutrality and subtracting this constant from each sweep. The resulting data follow the expected $\rho_{xy} = B/ne$

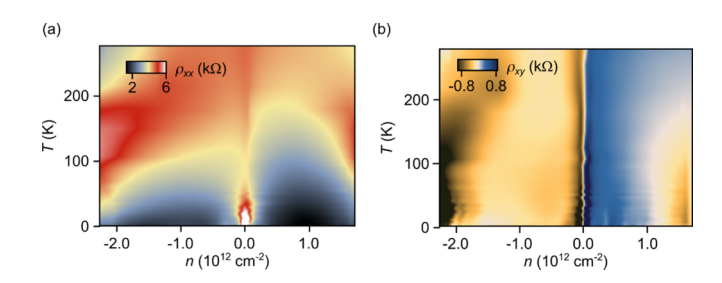


FIG. 5. (a) Color plot of resistivity ρ_{xx} vs temperature T and gate voltage V_g taken from sample D2. (b) Color plot of resistivity ρ_{xy} vs T and V_g taken at a magnetic field B = 0.2 T from sample D2.

behavior close to charge neutrality. For samples D1 and D3, ρ_{xy} was obtained using Onsager symmetrization (switching the current and voltage probes to isolate the measured ρ_{xy} component that is odd in B) as in, for example, Ref. [13].

APPENDIX B: CONDUCTIVITIES FROM LINEARIZED BOLTZMANN EQUATION

Boltzmann transport theory of quasiparticle transport is valid in the regime $k_F l \gg 1$, where k_F is the Fermi momentum and l the mean-free path. Strange metals often—but not always—violate the MIR limit $k_F l \approx 1$. If that were the case, one cannot justify using Boltzmann theory to understand the data.

A natural question to ask is if this is the case with TBG. To answer that, recall that, in 2D, $k_F l$ can be estimated directly from observed resistivity as $\rho_{xx} \approx h/e^2$ ($k_F l$), where $h/e^2 = 25.81 \text{ k}\Omega$ is the von Klitzing constant. We find that, even at the highest temperatures (100 K), up to which linear resistivity is observed in our TBG samples, the estimates of $k_F l$ range from 5 to 15.

It is thus *a priori* reasonable to use Boltzmann theory and ask if it can explain the data. We note, however, that at the end of our analysis, we will conclude that a Boltzmann theory based on quasiparticle transport is not able to account for the observed temperature dependence of both $\rho_{xx}(T)$ and $\rho_{xy}(T)$, at least using any known quasiparticle scattering mechanisms.

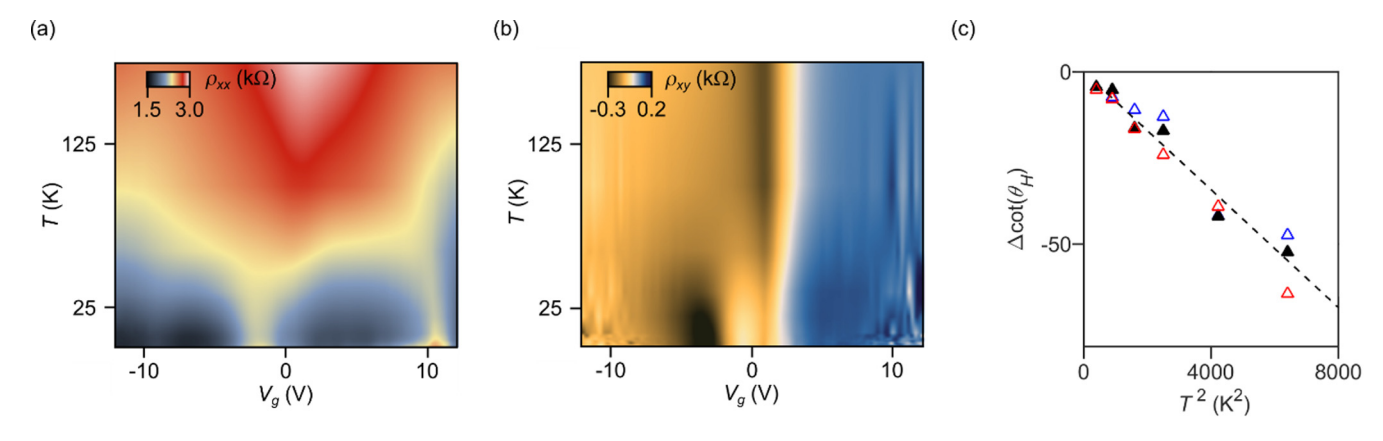


FIG. 6. (a) Color plot of resistivity ρ_{xx} vs temperature T and gate voltage V_g taken from sample D3. (b) Color plot of resistivity ρ_{xy} vs T and V_g taken at a magnetic field B=0.3 T from sample D3. (c) Change in the cotangent of the Hall angle from its low-temperature value vs T^2 for hole doping near half-filling for device D1. Densities are -1.7×10^{-12} , -1.66×10^{-12} , and -1.6×10^{-12} cm⁻² for blue, black, and red triangles, respectively. Solid triangles correspond to half-filling.

Next, we review the standard derivations for the longitudinal and Hall conductivities using the linearized Boltzmann equation within the relaxation time approximation. The distribution function f_{mk} for electrons in band m with crystal momentum k is obtained by solving the Boltzmann equation

$$\frac{e}{\hbar} (E + v_{mk} \times B) \cdot \nabla_k f_{mk} = -\frac{\left(f_{mk} - f_{mk}^0\right)}{\tau_{mk}}.$$
 (B1)

Here, $E = E \hat{x}$ and $B = B(-\hat{z})$ are the external fields, $v_{mk} = \hbar^{-1} \nabla_k \varepsilon_{mk}$ is the band velocity, $f_{mk}^0 = f^0(\varepsilon_{mk})$ is the Fermi function, and τ_{mk} is a phenomenological scattering time. Writing $f_{mk} = f_{mk}^0 + g_{mk}$ and keeping terms to linear order in E, we find

$$\left[1 + \frac{e}{\hbar} \tau_{mk} (\mathbf{v}_{mk} \times \mathbf{B}) \cdot \nabla_{\mathbf{k}}\right] g_{mk} = e \tau_{mk} (\mathbf{E} \cdot \mathbf{v}_{mk}) \left(-\frac{\partial f_{mk}^{0}}{\partial \varepsilon_{mk}}\right).$$
(B2)

We solve for g_{mk} by inverting the operator on the left-hand side above and keeping terms up to first order in \boldsymbol{B} (weak-field limit). We thus find

$$g_{mk} = \left(1 - \frac{e}{\hbar} \tau_{mk} (\mathbf{v}_{mk} \times \mathbf{B}) \cdot \nabla_k + \ldots\right)$$
$$\times \left(e \tau_{mk} (\mathbf{E} \cdot \mathbf{v}_{mk}) \left(-\frac{\partial f_{mk}^0}{\partial \varepsilon_{mk}}\right)\right)$$
(B3)

from which we obtain the current

$$J = e \sum_{l} v_{mk} g_{mk}.$$
 (B4)

We then calculate the conductivity

$$\begin{pmatrix} J_x \\ J_y \end{pmatrix} = \begin{pmatrix} \sigma_{xx} & \sigma_{xy} \\ -\sigma_{xy} & \sigma_{yy} \end{pmatrix} \begin{pmatrix} E \\ 0 \end{pmatrix}, \tag{B5}$$

to find

$$\sigma_{xx} = \frac{e^2}{h} \sum_{mk} \left(-\frac{\partial f_{mk}^0}{\partial \varepsilon_{mk}} \right) (v_{mk}^x)^2 \tau_{mk}, \tag{B6}$$

and

$$\sigma_{xy} = e^2 \left(\frac{eB}{\hbar}\right) \sum_{mk} \left(-\frac{\partial f_{mk}^0}{\partial \varepsilon_{mk}}\right) \left(v_{mk}^y \tau_{mk}\right) \times \left(v_{mk}^y \frac{\partial}{\partial k_x} - v_{mk}^x \frac{\partial}{\partial k_y}\right) \left(v_{mk}^x \tau_{mk}\right). \tag{B7}$$

Since experiments measure resistivities, we invert the conductivity matrix to find

$$\rho_{xx}(B=0) = \frac{1}{\sigma_{xx}}, \quad \rho_{xy} = -\frac{\sigma_{xy}}{\sigma_{xx}^2 + \sigma_{xy}^2} \approx -\frac{\sigma_{xy}}{\sigma_{xx}^2}.$$
 (B8)

TBG has four bands (2 spin \times 2 valley) crossing the chemical potential at any given filling of the narrow bands. We simply consider this using a degeneracy factor of four in the equations above.

APPENDIX C: BAND STRUCTURE

We need a model band structure to calculate the resistivities, and there are many available in the literature [27,28,36–38]. The continuum model of Bistritzer and McDonald correctly predicted the nearly flat bands at the magic angle but ignores lattice relaxation effects that lead to a large gap between the flat bands and higher bands. We use the band structure of Carr *et al.* [27], which includes the effects of lattice relaxation and uses maximally localized Wannier functions that respect the symmetries of TBG and the fragile topology of its electronic structure. Additionally, this model can be used for arbitrary twist angles, even away the magic angle.

We show how the band structure of TBG permits us to understand two distinct qualitative aspects of the transport data: (i) nonmonotonic T dependence of ρ_{xx} and (ii) variation of the low-temperature ρ_{xy} with density.

- (i) Nonmonotonicity of $\rho_{xx}(T)$: As already noted above, a realistic energy gap between the narrow bands and higher bands is built into the band structure of Carr *et al.* [27]; see Fig. 7(a). The Fermi occupancy factor in Eq. (B6) broadens with increasing temperature, and eventually, carriers in the higher band begin to contribute to transport, as shown in Fig. 3(b) of the main text. This leads to an eventual decrease in the resistivity at high T, with a peak near 150 K (for the parameters shown). This corresponds to half-filling on the electron-doped side of charge neutrality, using the bare band structure of Carr *et al.* [27] for the angle 1.12° relevant to our device D1. In this simple picture, the temperature at which the resistivity peak occurs should increase upon doping away from half-filling toward charge neutrality. This is indeed observed in the data shown in Fig. 3(a) of the main text.
- (ii) Doping dependence of low-temperature ρ_{xy} : We will see below that the Boltzmann approach cannot account for the T dependence of ρ_{xy} ; however, it can say something useful about the doping dependence when the temperature $T \ll$ bandwidth. In this limit, the k sums in Eqs. (B6) and (B7) are dominated by states near the Fermi surface (FS). Next, we convert the sum over k to an integral over energy together with a density of states $N(\varepsilon)$. If we further assume $\tau_{mk} = \tau(\varepsilon_{mk})$, we get the standard results [39]

$$\sigma_{xx} = 2 e^2 N(0) v_F^2 \tau$$
 and $\sigma_{xy} = (\omega_c \tau) \sigma_{xx}$, (C1)

where N(0) is the density of states at the Fermi level, v_F is the velocity averaged over the FS, given by $v_F^2 = \langle v_k^2 \rangle_{k \in FS}$, and τ is the relaxation time at the Fermi energy. The spin and valley degeneracy of four times $\frac{1}{2}$ (in 2D) accounts for the numerical prefactor in ρ_{xx} . In the Hall conductivity, we use the cyclotron frequency $\omega_c = eB/m^*$, with the effective mass m^* given by the "average curvature" of the FS

$$\frac{1}{m^*} = \frac{\left\langle \sum_{ij} v_k^i \left\{ \text{Tr}[M^{-1}(k)] \delta_{ij} - M_{ij}^{-1}(k) \right\} v_k^j \right\rangle_{k \in \text{FS}}}{\left\langle \sum_{ij} v_k^i (\delta_{ij}) v_k^j \right\rangle_{k \in \text{FS}}}, \quad (C2)$$

where $M_{ij}^{-1}(\mathbf{k}) = \hbar^{-2} \partial_i \partial_j \varepsilon(\mathbf{k})$. For $\varepsilon \sim |\mathbf{k}|^n$ in 2D, we can derive the relation $m^* v_F = \hbar k_F$, which is particularly useful for Dirac (n = 1) and parabolic (n = 2) dispersions.

It is clear from these results that the sign of Hall resistivity in Eq. (B8) is determined by that of m^* , which changes sign at

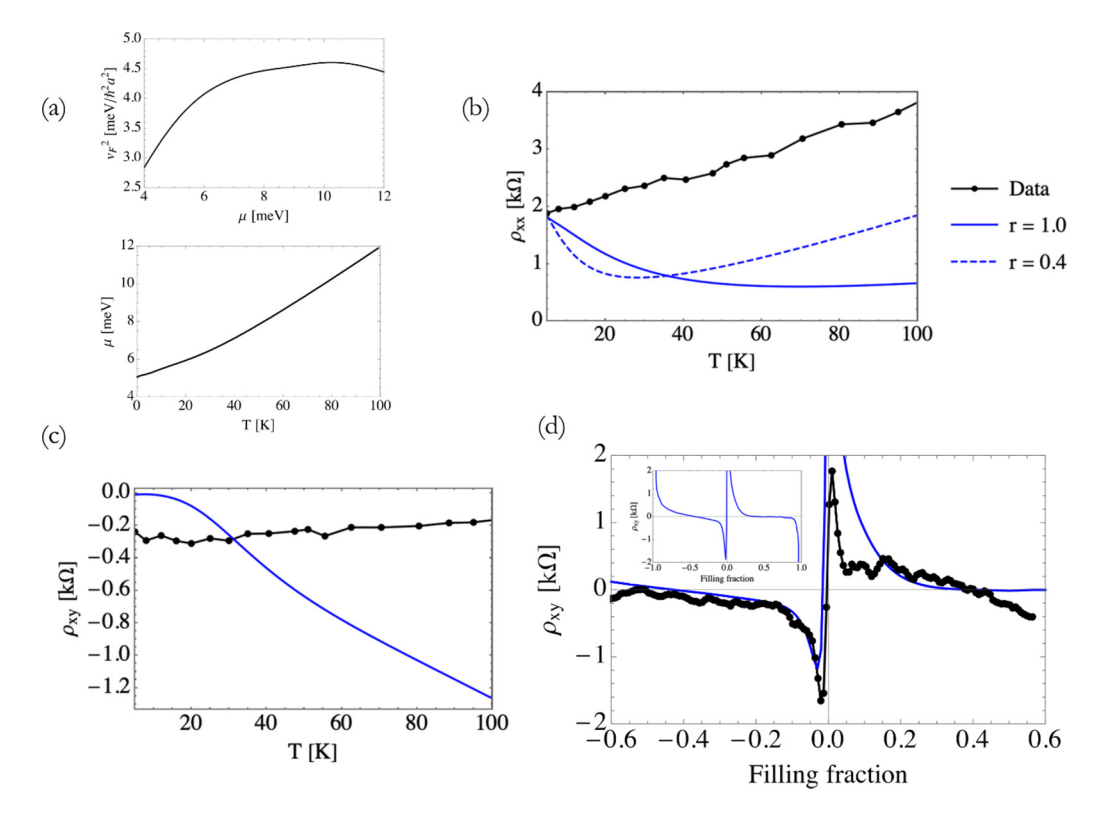


FIG. 7. (a) Trend of Fermi velocity squared vs chemical potential. In the range 4–10 meV, v_F increases with μ . $\mu(T)$ itself increases with temperature. This results in a bigger Fermi velocity which increases conductivity and decreases resistivity. The phenomenon is more pronounced for smaller bandwidths. (b) Numerically calculated resistivity vs temperature. Model calculations (blue) show nonmonotonicity which is not observed in the data (black). A renormalization factor can change the minima but cannot get rid of nonmonotonicity. Strength of scattering rate is 20 and 0.45 meV for r=1.0 and 0.4, respectively. (c) Temperature dependence for Hall resistivity, which mainly comes from the derivative of the Fermi function. However, the dependence is wrong. (d) Density dependence of Hall resistivity for D2 at low temperatures. Inset: Density dependence for all filling fractions of the narrow bands.

a Lifshitz transition where the system goes from a particlelike to a holelike FS. The zero crossing of ρ_{xy} can thus reveal important details about the band structure. We show in Fig. 7(d) that our choice of band structure captures this feature of the data.

APPENDIX D: IMPURITY SCATTERING IN NARROW BANDS

Elastic scattering from impurity scattering is usually invoked to account for the temperature-independent resistivity at low T. However, one might ask if impurity scattering in a very narrow band system can by itself lead to nontrivial T dependence in transport. While we will see that this is true in principle, it cannot explain any of the observed anomalies.

The elastic scattering rate of impurities is given by the Fermi golden rule expression

$$\Gamma_{mk} = \frac{\hbar}{\tau_{mk}} = 2\pi \sum_{m'k'} |M_{mk,m'k'}|^2 \delta(\varepsilon_{mk} - \varepsilon_{m'k'}), \quad (D1)$$

where $M_{mk,m'k'}$ is the impurity matrix element for scattering from the electron state (m,k) to (m',k'). For a structureless

matrix element, this simplifies to

$$\frac{1}{\tau_{mk}} = \frac{2\pi}{\hbar} n_{\text{imp}} U^2 N(\varepsilon_{mk}), \tag{D2}$$

where $n_{\rm imp}$ is the density of impurities, U is the strength of impurity potential, and $N(\varepsilon_{mk})$ is the density of states (DOS). The scattering rate is thus T independent but depends on the DOS, which is determined by the band structure. Using this result in Eq. (B6), we see that there are two factors that contribute to temperature dependence: (i) the T dependence of chemical potential $\mu(T)$ for a given density [see Fig. 7(a)] and (ii) the derivative of the Fermi function which has a height $\sim 1/T$ and width $\sim T$.

At high temperatures compared with μ and the bandwidth, the sum in Eq. (B6) extends to all states in the band, and the 1/T prefactor from $(-\frac{\partial f_{mk}^0}{\partial \varepsilon_{mk}})$ dominates the conductivity. This leads to a linear in T resistivity. However, this linear T resistivity does not persist down to low temperatures. At low temperatures compared with μ and the bandwidth, we can approximate $(-\frac{\partial f_{mk}^0}{\partial \varepsilon_{mk}}) \approx \delta(\varepsilon_{mk} - \mu)$ in Eq. (B6), and then $\mu(T)$ controls the T dependence of the resistivity. As μ increases with T, so does the Fermi velocity, and this leads to a decrease in resistivity with increasing T, as shown in Fig. 7(b). However, we note that the variation of the Fermi velocity with chemical potential depends on the details of the band structure

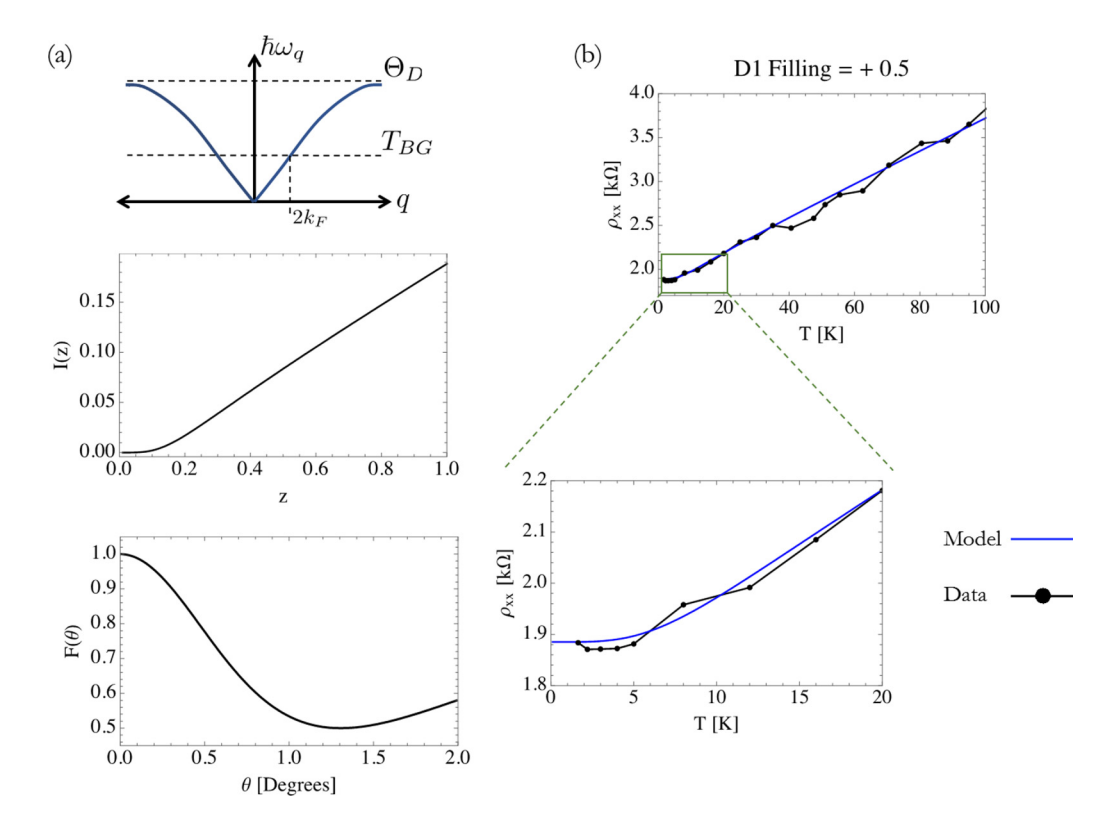


FIG. 8. (a) Schematic phonon dispersion showing the difference between Debye temperature and Bloch-Gruneisen temperature for a system with small density. Band structure factor $F(\theta)$ and Bloch-Gruneisen integral I(z) in Eq. (E2). I(z) is linear for $z \gg 1$, and the linearity sets in at $z \approx 0.25$. This gives $T_{\min} = T_{BG}/4$. $F(\theta)$ is a number bounded between 0.5 and 1. (b) Phonon model fit (blue) to data (black) for device D2. The model captures both slope and early onset of linearity with $v_F^*/v_F = 0.057$.

and is hence a nonuniversal feature. (In conventional metals, where bandwidth $W \approx 10^4$ K, the effects we are discussing are utterly negligible.)

The upshot of this analysis is that these two effects together can lead to a nontrivial T dependence in a very narrow band even from a T-independent impurity scattering rate but not one that can explain the observed data in TBG. In Fig. 7(b), we show an (unsuccessful) attempt to describe the linear T data over some range of temperatures using such an approach. The strength of scattering is fixed by matching the T=0 resistivity. We see that, renormalizing the Carr et al. [27] band dispersion $\varepsilon_{mk} \rightarrow r\varepsilon_{mk}$ by a factor of r=0.4, we can "fit" the slope of the linear T regime between 40 and 100 K, but then we also get a low-T upturn <40 K from the $\mu(T)$ effect described above. Band renormalization can be used to tune the temperature of this crossover, but the overall nonmonotonicity is robust.

The temperature dependence of $\rho_{xy}(T)$ further supports this conclusion argument. Narrow band effects, arising from the derivative of the Fermi function, lead to $|\rho_{xy}| \approx T$, as shown in Fig. 7(c). The experimental data clearly have a different temperature dependence.

Therefore, despite the subtleties of very narrow band systems, impurities alone fail to explain the observed data in TBG. In fact, the observed monotonic behavior of $\rho_{xx}(T)$ implies that the T dependence arising from Fermi factors is not relevant for TBG, and one must look at the T dependence of the scattering rates in Eqs. (B6) and (B7) to understand the data.

APPENDIX E: ELECTRON-PHONON SCATTERING: LONGITUDINAL RESISTIVITY

Next, we turn to acoustic phonon scattering, which accounts for linear T resistivity in metals over a range of temperatures $T_{\min} < T < T_{\max}$. Here, T_{\min} is usually a fraction of the Debye temperature Θ_D but can be much smaller in low-density systems (see below), while T_{\max} is essentially determined by the MIR criterion $k_F l(T_{\max}) \approx 1$.

We emphasize that electron-phonon scattering is clearly not responsible for the linear T resistivity in strongly correlated materials that are dubbed strange metals. In these systems, the MIR criterion is violated, with no observed $T_{\rm max}$, and at the same time, $T_{\rm min}$ is too low to be explained using phonons. TBG is different on both counts. First, as discussed in Sec. I, the MIR criterion is never violated in TBG, so there is no problem with $T_{\rm max}$. In fact, at high T, other bands come into play, as discussed in Sec. III. Further, as emphasized by Wu *et al.* [22], $T_{\rm min}$ is not an issue for ρ_{xx} in TBG either; see below. We agree with these authors that one can understand $\rho_{xx}(T)$ in terms of electron-phonon scattering; however, we will show that this mechanism cannot explain the observed Hall response.

The onset T_{\min} of the linear T scattering rate is controlled by the Bloch-Grüneisen temperature $k_BT_{BG} = \hbar v_{\rm ph} |\Delta k|_{\rm max} = \hbar v_{\rm ph} 2k_F$, where $2k_F$ is the maximum momentum transfer across the FS; see Fig. 8(a). In conventional metals (with $k_F \approx \pi/a$) T_{BG} is a fraction of the Debye temperature Θ_D . However, in a low-density system, we see that T_{BG} can be

parametrically smaller than Θ_D . For $T \gg T_{BG}$, the phonon occupation $n(\omega) \approx T/T_{BG}$, and this in turn leads to an electron-phonon scattering rate $\Gamma \approx T$.

This phenomenon has been studied in detail in Dirac materials like graphene [40], where for small densities and $T \gg T_{BG}$,

$$\rho_{xx} = \frac{\pi}{e^2 \hbar \ v_F^2} \left[\frac{1}{\rho_m} \left(\frac{D}{v_{\rm ph}} \right)^2 k_B T \right]. \tag{E1}$$

Here, D is the deformation potential (electron-phonon coupling), ρ_m the mass density, and v_F the Dirac velocity. (Here, the scattering rate is the quantity in square brackets.) The model has been extended to TBG by including the renormalization of the Dirac velocity and changes in electron-phonon matrix elements. As shown in eq. (2) of Wu *et al.* [22], the resistivity is then given by

$$\rho_{xx} = \frac{4}{e^2 (v_F^*)^2} \left[F(\theta) \frac{1}{\rho_m} \left(\frac{D}{v_{\text{ph}}} \right)^2 (v_{\text{ph}} k_F) I \left(\frac{T}{T_{BG}} \right) \right]. \quad (E2)$$

Here, the dimensionless functions $F(\theta)$, coming from the matrix element of electron-phonon Hamiltonian, and I(z) given in terms of a definite integral, are the same as those defined in Ref. [22]; their numerical values are plotted in Fig. 8(a). We followed the procedure outlined in their appendix A to calculate $F(\theta)$ for $\theta=1.12^\circ$. All other factors were taken to be the same as that of monolayer graphene, keeping v_F^* as the only fit parameter. The best fit to our experimental data was obtained with $v_F^*/v_F\approx 0.057$, where $v_F=10^6$ m/s is the Dirac velocity of monolayer graphene. This is very close to the prediction of the continuum model $(v_F^*/v_F\approx 0.05)$.

As emphasized by Wu *et al.* [22], electron-phonon scattering is the simplest mechanism that explains both resistivity slope ($\sim 100~\Omega/\mathrm{K}$) and the early onset of linear T resistivity ($\sim 5~\mathrm{K}$) within a conventional Boltzmann formalism. We show next that the same model fails to provide even a qualitative explanation of the T dependence of the Hall response.

APPENDIX F: HALL RESPONSE FROM ELECTRON-PHONON SCATTERING

We next show that phonons, and indeed Boltzmann transport, simply fail to explain the temperature dependence of $\cot \Theta_H$. We see from Eq. (C1) that

$$\cot \Theta_H = (\omega_c \tau)^{-1}, \tag{F1}$$

is a general consequence of Boltzmann transport since the same scattering mechanism impacts both σ_{xx} and σ_{xy} . Thus, ρ_{xx} and cot Θ_H share the same $1/\tau$ dependence and, hence, the same temperature dependence.

We note that, in this paper, we plot

$$\Delta \cot \Theta_H = \cot \Theta_H(T) - \cot \Theta_H(0),$$
 (F2)

motivated by Matthiessen's rule: $1/\tau$ is the sum of the impurity scattering rate $1/\tau(T=0)$ plus the inelastic scattering rate. Thus, $\Delta \cot \Theta_H$ allows us to focus on the latter and ignore the T=0 impurity contribution.

APPENDIX G: MULTIBAND MOMENTUM DEPENDENT SCATTERING

Any inelastic scattering mechanism (including electronphonon scattering) that explains linear T resistivity within a quasiparticle picture has a rate that can be written as

$$\Gamma_{m,k} = \frac{\hbar}{\tau_{m,k}} = k_B T \ \Phi_{m,k}, \tag{G1}$$

where Φ_{mk} depends on the band structure and scattering matrix elements but not on T. When the k sums in the Boltzmann results are dominated by FS contributions, only the value of Φ_{mk} evaluated at the FS affects the prefactors, but the temperature dependence of $\cot \Theta_H$ is simply linear in T. This is clearly in qualitative disagreement with the experimentally observed $\cot \Theta_H \approx T^2$.

We emphasize that observed behavior cannot be attributed to multiband effects in the Boltzmann theory of Hall response (see, e.g., sec. 12.2 of Ref. [41]). The resistivity clearly requires that the different bands have the same linear T dependence in the scattering rates, even if the numerical coefficients were to be band dependent [see Eq. (G1)]. Then even though the final multiband result for the Hall resistivity is complicated, the T dependence simply cancels out.

In conclusion, while acoustic phonon scattering can account for the strange linear T resistivity, it fails to explain the quadratic behavior of $\cot \Theta_H$. The failure is not limited to phonons but is equally problematical for any scattering mechanism within Boltzmann theory. Therefore, we argue that TBG is indeed a strange metal, whose strangeness is perhaps not directly visible in the longitudinal resistivity but is emphasized by considering the cotangent of Hall angle together with ρ_{xx} .

^[1] J. A. N. Bruin, H. Sakai, R. S. Perry, and A. P. Mackenzie, Similarity of scattering rates in metals showing *T*-linear resistivity, Science **339**, 804 (2013).

^[2] A. Legros, S. Benhabib, W. Tabis, F. Laliberté, M. Dion, M. Lizaire, B. Vignolle, D. Vignolles, H. Raffy, Z. Z. Li, P. Auban-Senzier, N. Doiron-Leyraud, P. Fournier, D. Colson, L. Taillefer, and C. Proust, Universal *T*-linear resistivity and Planckian dissipation in overdoped cuprates, Nat. Phys. 15, 142 (2019).

^[3] P. T. Brown, D. Mitra, E. Guardado-Sanchez, R. Nourafkan, A. Reymbaut, C.-D. Hébert, S. Bergeron, A. M. S. Tremblay, J. Kokalj, D. A. Huse, P. Schauß, and W. S. Bakr, Bad metallic

transport in a cold atom Fermi-Hubbard system, Science **363**, 379 (2019).

^[4] S. A. Hartnoll, A. Lucas, and S. Sachdev, *Holographic Quantum Matter* (MIT Press, Cambridge, MA, 2018).

^[5] T. R. Chien, Z. Z. Wang, and N. P. Ong, Effect of Zn Impurities on the Normal-State Hall Angle in Single-Crystal YBa₂Cu_{3-x}Zn_xO_{7-δ}, Phys. Rev. Lett. 67, 2088 (1991).

^[6] A. Carrington, A. P. Mackenzie, C. T. Lin, and J. R. Cooper, Temperature Dependence of the Hall Angle in Single-Crystal YBa₂(Cu_{1-x}Co_x)₃O_{7-δ}, Phys. Rev. Lett. 69, 2855 (1992).

^[7] A. L. Sharpe, E. J. Fox, A. W. Barnard, J. Finney, K. Watanabe, T. Taniguchi, M. A. Kastner, and D. Goldhaber-

- Gordon, Emergent ferromagnetism near three-quarters filling in twisted bilayer graphene, Science 365, 605 (2019).
- [8] Y. Cao, V. Fatemi, A. Demir, S. Fang, S. L. Tomarken, J. Y. Luo, J. D. Sanchez-Yamagishi, K. Watanabe, T. Taniguchi, E. Kaxiras, R. C. Ashoori, and P. Jarillo-Herrero, Correlated insulator behaviour at half-filling in magic-angle graphene superlattices, Nature 556, 80 (2018).
- [9] Y. Cao, V. Fatemi, S. Fang, K. Watanabe, T. Taniguchi, E. Kaxiras, and P. Jarillo-Herrero, Unconventional superconductivity in magic-angle graphene superlattices, Nature 556, 43 (2018).
- [10] M. Yankowitz, S. Chen, H. Polshyn, Y. Zhang, K. Watanabe, T. Taniguchi, D. Graf, A. F. Young, and C. R. Dean, Tuning superconductivity in twisted bilayer graphene, Science 363, 1059 (2019).
- [11] E. Codecido, Q. Wang, R. Koester, S. Che, H. Tian, R. Lv, S. Tran, K. Watanabe, T. Taniguchi, and F. Zhang, M. Bockrath, and C. N. Lau, Correlated insulating and superconducting states in twisted bilayer graphene below the magic angle, Sci. Adv. 5, eaaw9770 (2019).
- [12] X. Lu, P. Stepanov, W. Yang, M. Xie, M. A. Aamir, I. Das, C. Urgell, K. Watanabe, T. Taniguchi, and G. Zhang, A. Bachtold, A. H. MacDonald, and D. K. Efetov, Superconductors, orbital magnets and correlated states in magic-angle bilayer graphene, Nature 574, 653 (2019).
- [13] M. Serlin, C. L. Tschirhart, H. Polshyn, Y. Zhang, J. Zhu, K. Watanabe, T. Taniguchi, L. Balents, and A. F. Young, Intrinsic quantized anomalous Hall effect in a moiré heterostructure, Science 367, 900 (2020).
- [14] Y. Xie, B. Lian, B. Jäck, X. Liu, C.-L. Chiu, K. Watanabe, T. Taniguchi, B. A. Bernevig, and A. Yazdani, Spectroscopic signatures of many-body correlations in magic-angle twisted bilayer graphene, Nature 572, 101 (2019).
- [15] Y. Choi, J. Kemmer, Y. Peng, A. Thomson, H. Arora, R. Polski, Y. Zhang, H. Ren, J. Alicea, and G. Refael, F. von Oppen, K. Watanabe, T. Taniguchi, and S. Nadj-Perge, Electronic correlations in twisted bilayer graphene near the magic angle, Nat. Phys. 15, 1174 (2019).
- [16] Y. Jiang, X. Lai, K. Watanabe, T. Taniguchi, K. Haule, J. Mao, and E. Y. Andrei, Charge order and broken rotational symmetry in magic-angle twisted bilayer graphene, Nature 573, 91 (2019).
- [17] A. Kerelsky, L. J. McGilly, D. M. Kennes, L. Xian, M. Yankowitz, S. Chen, K. Watanabe, T. Taniguchi, J. Hone, C. Dean, A. Rubio, and A. N. Pasupathy, Maximized electron interactions at the magic angle in twisted bilayer graphene, Nature 572, 95 (2019).
- [18] Y. Cao, D. Chowdhury, D. Rodan-Legrain, O. Rubies-Bigorda, K. Watanabe, T. Taniguchi, T. Senthil, and P. Jarillo-Herrero, Strange Metal in Magic-Angle Graphene with near Planckian Dissipation, Phys. Rev. Lett. 124, 076801 (2020).
- [19] J. Zaanen, Why the temperature is high, Nature 430, 512 (2004).
- [20] H. Polshyn, M. Yankowitz, S. Chen, Y. Zhang, K. Watanabe, T. Taniguchi, C. R. Dean, and A. F. Young, Large linear-intemperature resistivity in twisted bilayer graphene, Nat. Phys. 15, 1011 (2019).
- [21] T.-F. Chung, Y. Xu, and Y. P. Chen, Transport measurements in twisted bilayer graphene: Electron-phonon coupling and Landau level crossing, Phys. Rev. B **98**, 035425 (2018).
- [22] F. Wu, E. Hwang, and S. Das Sarma, Phonon-induced giant linear-in-*T* resistivity in magic angle twisted bilayer graphene:

- Ordinary strangeness and exotic superconductivity, Phys. Rev. B **99**, 165112 (2019).
- [23] K. Kim, A. DaSilva, S. Huang, B. Fallahazad, S. Larentis, T. Taniguchi, K. Watanabe, B. J. LeRoy, A. H. MacDonald, and E. Tutuc, Tunable moiré bands and strong correlations in small-twist-angle bilayer graphene, Proc. Natl. Acad. Sci. USA 114, 3364 (2017).
- [24] K. Kim, M. Yankowitz, B. Fallahazad, S. Kang, H. C. P. Movva, S. Huang, S. Larentis, C. M. Corbet, T. Taniguchi, K. Watanabe, S. K. Banerjee, B. J. LeRoy, and E. Tutuc, van der Waals heterostructures with high accuracy rotational alignment, Nano Lett. 16, 1989 (2016).
- [25] D. B. Farmer, V. Perebeinos, Y.-M. Lin, C. Dimitrakopoulos, and P. Avouris, Charge trapping and scattering in epitaxial graphene, Phys. Rev. B 84, 205417 (2011).
- [26] C. R. Dean, A. F. Young, I. Meric, C. Lee, L. Wang, S. Sorgenfrei, K. Watanabe, T. Taniguchi, P. Kim, K. L. Shepard, and J. Hone, Boron nitride substrates for high-quality graphene electronics, Nat. Nanotechnol. 5, 722 (2010).
- [27] S. Carr, S. Fang, Z. Zhu, and E. Kaxiras, Exact continuum model for low-energy electronic states of twisted bilayer graphene, Phys. Rev. Res. 1, 013001 (2019).
- [28] R. Bistritzer and A. H. MacDonald, Moiré bands in twisted double-layer graphene, Proc. Nat. Acad. Sci. USA 108, 12233 (2011).
- [29] J. M. B. Lopes dos Santos, N. M. R. Peres, and A. H. Castro Neto, Continuum model of the twisted graphene bilayer, Phys. Rev. B 86, 155449 (2012).
- [30] A. J. M. Giesbers, U. Zeitler, M. I. Katsnelson, L. A. Ponomarenko, T. M. G. Mohiuddin, and J. C. Maan, Temperature dependence of the quantum Hall effect in graphene, Physica E 40, 1089 (2008).
- [31] T. Ohta, J. T. Robinson, P. J. Feibelman, A. Bostwick, E. Rotenberg, and T. E. Beechem, Evidence for Interlayer Coupling and Moiré Periodic Potentials in Twisted Bilayer Graphene, Phys. Rev. Lett. 109, 186807 (2012).
- [32] H. v. Löhneysen, A. Rosch, M. Vojta, and P. Wölfle, Fermiliquid instabilities at magnetic quantum phase transitions, Rev. Mod. Phys. 79, 1015 (2007).
- [33] T. Shibauchi, A. Carrington, and Y. Matsuda, A quantum critical point lying beneath the superconducting dome in iron pnictides, Annu. Rev. Condens. Matter Phys. 5, 113 (2014).
- [34] C. Proust and L. Taillefer, The remarkable underlying ground states of cuprate superconductors, Annu. Rev. Condens. Matter Phys. **10**, 409 (2019).
- [35] B. Michon, C. Girod, S. Badoux, J. Kačmarčík, Q. Ma, M. Dragomir, H. A. Dabkowska, B. D. Gaulin, J. S. Zhou, S. Pyon, T. Takayama, H. Takagi, S. Verret, N. Doiron-Leyraud, C. Marcenat, L. Taillefer, and T. Klein, Thermodynamic signatures of quantum criticality in cuprate superconductors, Nature 567, 218 (2019).
- [36] M. Koshino, N. F. Q. Yuan, T. Koretsune, M. Ochi, K. Kuroki, and L. Fu, Maximally Localized Wannier Orbitals and the Extended Hubbard Model for Twisted Bilayer Graphene, Phys. Rev. X 8, 031087 (2018).
- [37] J. Kang and O. Vafek, Symmetry, Maximally Localized Wannier States, and a Low-Energy Model for Twisted Bilayer Graphene Narrow Bands, Phys. Rev. X 8, 031088 (2018).

- [38] H. C. Po, L. Zou, T. Senthil, and A. Vishwanath, Faithful tight-binding models and fragile topology of magic-angle bilayer graphene, Phys. Rev. B **99**, 195455 (2019).
- [39] J. M. Ziman, *Principles of the Theory of Solids* (Cambridge University Press, Cambridge, 1972).
- [40] S. Das Sarma, S. Adam, E. H. Hwang, and E. Rossi, Electronic transport in two-dimensional graphene, Rev. Mod. Phys. **83**, 407 (2011).
- [41] J. M. Ziman, *Electrons and Phonons: The Theory of Transport Phenomena in Solids* (Oxford University Press, Oxford, 2001).